Effects of Buoyancy and Wind Forcing on Southern Ocean Climate Change

JIA-RUI SHI, LYNNE D. TALLEY, AND SHANG-PING XIE

Scripps Institution of Oceanography, University of California San Diego, La Jolla, California

WEI LIU

Department of Earth and Planetary Sciences, University of California Riverside, Riverside, California

SARAH T. GILLE

Scripps Institution of Oceanography, University of California San Diego, La Jolla, California

(Manuscript received 24 November 2019, in final form 13 July 2020)

ABSTRACT

Observations show that since the 1950s, the Southern Ocean has stored a large amount of anthropogenic heat and has freshened at the surface. These patterns can be attributed to two components of surface forcing: poleward-intensified westerly winds and increased buoyancy flux from freshwater and heat. Here we separate the effects of these two forcing components by using a novel partial-coupling technique. We show that buoyancy forcing dominates the overall response in the temperature and salinity structure of the Southern Ocean. Wind stress change results in changes in subsurface temperature and salinity that are closely related to intensified residual meridional overturning circulation. As an important result, we show that buoyancy and wind forcing result in opposing changes in salinity: the wind-induced surface salinity increase due to upwelling of saltier subsurface water offsets surface freshening due to amplification of the global hydrological cycle. Buoyancy and wind forcing further lead to different vertical structures of Antarctic Circumpolar Current (ACC) transport change; buoyancy forcing causes an ACC transport increase (3.1 ± 1.6 Sv; $1\ \text{Sv} \equiv 10^6\ \text{m}^3\ \text{s}^{-1}$) by increasing the meridional density gradient across the ACC in the upper 2000 m, while the wind-induced response is more barotropic, with the whole column transport increased by 8.7 ± 2.3 Sv. While previous research focused on the wind effect on ACC intensity, we show that surface horizontal current acceleration within the ACC is dominated by buoyancy forcing. These results shed light on how the Southern Ocean might change under global warming, contributing to more reliable future projections.

1. Introduction

Observations have revealed a complex set of changes in the Southern Ocean over the past few decades. The most pronounced is subsurface warming in the Southern Ocean (Purkey and Johnson 2010; Rhein et al. 2013; Roemmich et al. 2015; Desbruyères et al. 2016; Cheng et al. 2016; Shi et al. 2018), which illustrates the important role of the Southern Ocean in slowing the global surface warming rate. This significant warming can be traced back to the 1950s (Gille 2002, 2008). A broad-scale salinity decrease in the surface, mode, and intermediate waters in the Southern Ocean has also occurred since 1950 (Durack and Wijffels 2010). The change in surface buoyancy flux, which is the combination of heat flux and freshwater flux, supports the temperature and salinity changes physically (Swart et al. 2018). Moreover, the Southern Ocean has experienced significant surface wind stress change (Swart and Fyfe 2012). In particular, observations show poleward-intensified westerly winds associated with a positive tendency of the southern annular mode (SAM) index (Thompson 2002; Marshall 2003), which has been found to be forced by both stratospheric ozone depletion (Gillett 2003; Waugh et al. 2013) and anthropogenic greenhouse gas emissions

Denotes content that is immediately available upon publication as open access.

Supplemental information related to this paper is available at the Journals Online website: https://doi.org/10.1175/JCLI-D-19-0877.s1.

Corresponding author: Jia-Rui Shi, jis190@ucsd.edu

DOI: 10.1175/JCLI-D-19-0877.1

(Fyfe and Saenko 2006). The observed poleward shift in Southern Hemisphere westerlies occurs mostly in austral summer and is compensated by opposing shifts in other seasons (Lee and Feldstein 2013; Swart et al. 2015).

Manabe et al. (1990) found in a modeling study that the Southern Ocean dominates anthropogenic heat uptake. Based on CMIP5 models, more than 70% of anthropogenic heat is absorbed by the Southern Ocean (south of 30°S, occupying 30% of global surface ocean area) during the historical period (Frölicher et al. 2015; Shi et al. 2018). In the Southern Ocean, deep water upwells along isopycnals that connect the deep ocean to the sea surface, where water masses can interact with the atmosphere, exchanging heat before returning to the ocean interior. Armour et al. (2016) showed that the upwelling of pristine, older deep water with stable temperature under a warming atmosphere leads to greater heat transfer to the ocean because of the increasing ocean–atmosphere temperature difference. Shi et al. (2018) showed that the compensating effects of greenhouse gases and anthropogenic aerosols in the Northern Hemisphere leads to small ocean heat uptake in the subpolar North Atlantic, resulting in dominance of the Southern Hemisphere in global ocean heat uptake. The subsurface warming or ocean heat content (OHC) increase in the Southern Ocean corresponds to enhanced ocean heat uptake at the surface (peaking around 55°–60°S), while most subsurface warming occurs farther equatorward, peaking around 40°–45°S (Roemmich et al. 2015; Frölicher et al. 2015; Armour et al. 2016). The equatorward displacement of maximum subsurface warming relative to maximum heat uptake is attributed to the background meridional overturning circulation (MOC), which redistributes the absorbed heat (Armour et al. 2016; Liu et al. 2018). The warmed water is advected northward by Ekman transport, eventually resulting in enhanced warming on the northern flank of the Antarctic Circumpolar Current (ACC) and delayed warming on the southern flank (Armour et al. 2016). Moreover, amplification of the global hydrological cycle, manifested as increased atmospheric freshwater fluxes over the high-latitude oceans, is an important factor driving the observed surface freshening of the Southern Ocean (Durack and Wijffels 2010; Helm et al. 2010; Durack et al. 2012). More recent studies suggest that the freshening also stems from equatorward wind-driven sea ice transport (Haumann et al. 2016) and enhanced Antarctic glacial melt (Jacobs 2002; Paolo et al. 2015; Bronselaer et al. 2018; Bintanja et al. 2013; Swart and Fyfe 2013).

Southern Ocean circulations, that is, the MOC and the ACC, are affected by the overlying strong westerly winds. Mesoscale eddies can offset the effects of surface wind stress change on the MOC and ACC due to eddy compensation and eddy saturation, respectively (Morrison and Hogg 2013). High-resolution ocean models show that wind-driven MOC intensification is partially compensated by an eddy-induced MOC; the compensating ratio is about 50% (Gent 2016). In addition, several modeling studies have shown that the ocean state approaches the fully eddy-saturated regime, with the response of ACC transport insensitive to wind perturbation (Meredith and Hogg 2006; Hallberg and Gnanadesikan 2006; Farneti et al. 2010). Similarly, the observationally based study of Böning et al. (2008) suggested that, because of eddy saturation, the ACC transport and associated isopycnal tilt are largely unaffected by the poleward-intensified westerly winds. Recent studies (Meredith et al. 2012; Dufour et al. 2012; Morrison and Hogg 2013) find that surface wind stress change is indeed capable of driving weak but significant changes in ACC transport, associated with changes in the zonal barotropic current rather than with changes in the density structure (Zika et al. 2013; Langlais et al. 2015).

To isolate the effect of wind forcing change on the Southern Ocean, several studies have used the wind pattern derived from global warming experiments as a perturbation (Fyfe et al. 2007; Spence et al. 2010). They find that poleward-intensified westerly winds enhance Southern Ocean warming north of the ACC and lead to cooling south of the ACC at depth, primarily controlling the spatial pattern of the warming signal. Buoyancy forcing change has also been shown to affect the Southern Ocean. For example, heating and/or freshening of the Southern Ocean can increase ocean stratification, allowing warming in the atmosphere to accelerate and ocean heat storage to slow (Russell et al. 2006). The surface intensified warming also results in a reduction in the diffusive and advective, southward and upward eddy heat transport (Morrison et al. 2016). Buoyancy forcing can also influence ACC transport by altering upper layer stratification and the cross-stream density gradient (Hogg 2010). Hence it is essential to understand the relative importance of wind and buoyancy forcing in Southern Ocean climate change and the fingerprint (forced response) of change associated with each forcing component.

In this study, we explore the respective effects of buoyancy and wind (momentum) forcing on transient climate change in the Southern Ocean by using partial-coupling model simulations (Liu et al. 2018) in which wind stress fields are prescribed. Fyfe et al. (2007) pioneered a similar approach to separating buoyancy and wind forcing effects, but their simple energy-balance model of the atmosphere limited the simulation skill, especially regarding the hydrological cycle and salinity. Liu et al. (2018) mainly focus on the Eulerian mean and eddy-induced MOC change due to buoyancy and wind forcing. Here, we examine the fingerprint of buoyancy and wind forcing in ocean circulation, temperature, salinity,

and sea ice changes in idealized experiments with quadrupled atmospheric CO_2. Previous studies largely focused on the response of the Southern Ocean to changes in westerly winds, whereas we find that buoyancy forcing dominates the overall response in the temperature and salinity structure of the Southern Ocean. Buoyancy forcing accounts for 80% of the total heat storage change within a quadrupled CO_2 experiment, and wind forcing accounts for the rest, the pattern of which is closely linked with the strengthened residual MOC due to intensified westerly winds. As an important result, we find that buoyancy and wind forcing have opposite impacts on salinity: surface salinity increase over the Southern Ocean driven by stronger wind-driven upwelling of saline waters in the MOC can substantially offset surface freshening due to a global water cycle amplification. Moreover, we find that the changes in subsurface temperature driven by buoyancy forcing can further intensify the horizontal (circumpolar) circulation due to a change in the meridional density gradient, whereas wind stress changes create a more barotropic increase in circumpolar transport. The surface horizontal velocity acceleration is primarily driven by buoyancy forcing. Understanding the relative responses to these two forcing changes is crucial to understanding observed long-term change in the Southern Ocean.

The rest of the paper is organized as follows. Section 2 describes the models, experiments, data, and methods used in this study. Section 3 discusses the response of Southern Ocean temperature to wind change and surface buoyancy forcing. Section 4 discusses the change of salinity and sea ice due to both forcing components. Section 5 further investigates the ACC response, including transport and position. Section 6 provides discussion and conclusions.

2. Data and methods

a. CESM and partial coupling experiments

We use the Community Earth System Model (CESM), version 1.0.5, from the National Center for Atmospheric Research (NCAR) (Hurrell et al. 2013). The model consists of the version 5 of the Community Atmosphere Model (CAM5), run at a nominal 2° resolution (1.9° latitude × 2.5° longitude) with 26 vertical layers, and version 2 of the Parallel Ocean Program (POP2), which has a nominal resolution of 0.5° in latitude and 1° in longitude over the Southern Ocean. The Community Land Model, version 4, and Community Ice Code, version 4, are coupled with the atmosphere and ocean model. The ocean model employs a temporally and spatially varying specification of the Gent–McWilliams (GM) eddy parameterization (Gent and McWilliams 1990). For tracers, such as temperature, the horizontal diffusion follows the Redi isoneutral diffusion operator as represented by the GM parameterization, and the vertical diffusion follows the K-profile parameterization (Large et al. 1994). NCAR CESM is widely used and has been extensively evaluated against observations and other climate models (Kay et al. 2015, 2016; Cheng and Zhu 2016; Bracegirdle et al. 2018; Beadling et al. 2019).

Here we employ a partial coupling technique (Lu and Zhao 2012; Liu et al. 2015, 2018) to isolate the effects of the wind-induced Southern Ocean climate change. In the partial coupling experiments, variables at the air–sea interface (e.g., wind stress) from fully coupled runs are prescribed in the ocean model in order to disable the targeted feedback. Here we use a fully coupled, preindustrial control run (CTRL) as the baseline run, which starts from the AD 1850 scenario. We also use a fully coupled, abruptly quadrupled CO_2 ($4 \times CO_2$) run, which branches from CTRL, with the atmospheric CO_2 concentration instantly quadrupled from the 1850 level and kept constant through the 90-yr simulation. Next, we conduct a suite of partial-coupling experiments with prescribed wind stress and surface wind speed from the above-mentioned fully coupled cases (CTRL and $4 \times CO_2$) at the daily frequency of air–sea coupling. Here, winds can affect surface heat uptake and interior ocean heat redistribution either by changing ocean circulation via momentum flux (dynamic effect) or by modifying ocean–atmosphere thermal coupling through the wind speed in the bulk formula of turbulent (latent and sensible) heat fluxes (thermal dynamic effect). Wind stress τ, wind speed w, and CO_2 level c are the variables of interest. To target climate response without wind change, we quadruple the atmospheric CO_2 level (c4) with prescribed wind stress (τ1) and speed (w1) from CTRL; we call this τ1w1c4 to specify wind from CTRL and CO_2 level from $4 \times CO_2$. The definition of each term is shown in Table 1. In sum, we have three partially coupled experiments: τ1w1c1, τ1w1c4, and τ4w1c4. The transient response of the Southern Ocean to wind stress change under quadrupled CO_2 can be obtained by taking the difference between the simulations with and without wind stress changes:

$$\mathrm{Wstr} = (\tau 4\mathrm{w}1\mathrm{c}4 - \tau 1\mathrm{w}1\mathrm{c}4). \quad (1)$$

The buoyancy forcing response can be obtained by taking the difference between the simulations with and without changing the external CO_2 forcing, while keeping the surface wind stress and speed from CTRL:

$$\mathrm{Buoy} = (\tau 1\mathrm{w}1\mathrm{c}4 - \tau 1\mathrm{w}1\mathrm{c}1). \quad (2)$$

Buoy includes effects due to changes in surface heat flux and freshwater flux. We have previously shown, using this partial coupling technique, that the surface wind speed effect on surface heat and freshwater fluxes has a minimal effect on Southern Ocean climate change (Liu et al. 2018). Therefore, in this paper, we focus on the

TABLE 1. Notations for partial-coupling experiments using NCAR CESM1. In partial coupling, wind stress and wind speed are shifted forward by one year.

Expt name	Note
τ1	Wind stress from CTRL
τ4	Wind stress from 4 × CO_2
w1	Wind speed from CTRL
c1	1 × CO_2 (preindustrial level) emission (CTRL)
c4	4 × CO_2 emission (4 × CO_2)
τ1w1c1	Partial coupling with CTRL variables
τ1w1c4	Partial coupling with quadrupled CO_2
τ4w1c4	Partial coupling with τ4 and quadrupled CO_2
CTRL	Fully coupled, preindustrial control run
4 × CO_2	Fully coupled, abruptly quadrupled CO_2

wind stress effect (Wstr) and the buoyancy forcing effect (Buoy), both of which we show have significant impacts. In this partial coupling technique, we represent the total effect (Total) as the linear sum of Wstr and Buoy:

$$\text{Total} = \text{Wstr} + \text{Buoy} = (\tau4\text{w1c4} - \tau1\text{w1c1}). \quad (3)$$

The experiments using from the partial-coupling experiments are summarized in Table 2.

Surface wind is coherent with other fields, such as surface heat flux. The coherence can intertwine the wind-induced and buoyancy-induced responses. To disrupt this coherence and to separate responses due to wind change and buoyancy flux change, wind stress and speed are shifted forward by one year during the partial coupling. In addition, the partial coupling technique can generate a climate drift by disrupting air–sea interaction. The climate drift due to partial coupling can be largely eliminated by computing the difference between partially coupled runs because the same drift is present in all runs. The responses for Total are compared with the fully coupled experiment (4 × CO_2 − CTRL; see Fig. S1 in the online supplemental material). The Total case largely reproduces 4 × CO_2 − CTRL in ocean temperature, salinity, and circumpolar velocity, with a discrepancy mainly at intermediate depth in salinity change. The similarities between the Total case and fully coupled run indicate that the overall effects can be largely represented by a linear combination of Buoy and Wstr [Eq. (3)]. We also compare the Southern Ocean temperature, salinity, and density structure in the partially coupled CESM simulation (τ1w1c1) with the mean state from Argo profiling float observations (2005–18; section 2c). The mean state from CESM agrees roughly with observations (Fig. S2). The zonal-mean CESM and Argo density structures are very similar (Fig. S2c). However, CESM shows steeper isothermal slopes in the ACC compared to Argo, resulting in deeper penetration of heat to the north of the ACC than is observed. The salinity minimum is located at a shallower depth in CESM than in Argo, which may confine the CESM salinity change within the upper layer. Last, the ACC volume transport through the Drake Passage from τ1w1c1 is 166.6 Sv (1 Sv ≡ 10^6 m^3 s^{-1}), which falls within the range (173.3 ± 10.7 Sv) observed from the cDrake experiment by Donohue et al. (2016). More details about the CESM1 model configuration and setup can be found in Liu et al. (2018). We analyze changes over years 41–90, which represents the slow (multidecadal) response (Ferreira et al. 2015) to wind and buoyancy forcing.

b. *FAFMIP experiment*

In addition to the CESM partial coupling experiments, this study also uses the output of the Flux-Anomaly-Forced Model Intercomparison (FAFMIP) experiments from four models: ACCESS-CM2 (Hirst et al. 2015), MIROC6 (Tatebe et al. 2019), MPI-ESM1.2-HR (Gutjahr et al. 2019), and MRI-ESM2.0 (Yukimoto et al. 2019). FAFMIP is part of phase 6 of the Coupled Model Intercomparison Project (CMIP6). The FAFMIP experiments, branched from preindustrial conditions (piControl), prescribe a set of surface flux perturbations for the ocean. These perturbations are obtained from the ensemble-mean changes simulated at the time of doubled CO_2 by CMIP5 AOGCMs under the

TABLE 2. Buoyancy and wind forcing effects derived from experiments using the CESM1 partial-coupling technique. The differences between individual pairs of partial-coupling experiments reveal the contributions from Buoy and Wstr. The total effect of wind and buoyancy forcing is Total (Buoy + Wstr, or τ4w1c4 − τ1w1c1).

Effects	Note	Derivation
Buoy	Buoyancy forcing effect	τ1w1c4 − τ1w1c1
Wstr	Wind forcing effect	τ4w1c4 − τ1w1c4
Total = Buoy + Wstr	Total effect	τ4w1c4 − τ1w1c1

1pctCO2 scenario (CO_2 increases by 1% each year). This study examines FAFMIP experiments: FAF-Wstr (faf-stress), imposing perturbation surface wind stress; FAF-Heat, imposing perturbation surface heat flux; and FAF-Water, imposing perturbation surface freshwater flux (Gregory et al. 2016). For FAF-Heat, the heat flux perturbation yields a strong negative feedback due to SST warming. To avoid this negative feedback and to require all of the prescribed heat flux perturbation to enter the ocean, Bouttes and Gregory (2014) used a passive tracer of ocean temperature to prevent the atmosphere from feeling the SST change due to the heat flux perturbation. More details about the treatment of heat flux perturbations can be found in Gregory et al. (2016).

All FAFMIP experiments considered here were run for 70 years. We show the anomalies of the 41–70-yr average relative to the climatology from piControl. In addition, we linearly combine the results from FAF-Heat and FAF-Water as FAF-Buoy to represent a buoyancy forcing experiment. FAF-All represents the sum of FAF-Wstr and FAF-Buoy. FAF-Wstr and our CESM Wstr runs may be directly compared to evaluate the model dependency. Because of the differences in the experimental design, however, further studies are needed to understand how to compare FAF-Buoy and our CESM Buoy runs.

c. Observations

We use temperature and salinity products from the *World Ocean Atlas 2018* (*WOA18*; https://www.nodc.noaa.gov/OC5/woa18/). *WOA18* is a uniformly formatted and quality-controlled dataset based on the World Ocean Database. Objectively analyzed climatologies of temperature and salinity (1955–64, 1965–74, 1975–84, and 2005–17) are used in this study. Long-term ocean temperature and salinity changes are calculated as the difference between the 2005–17 mean and the mean over the 1955–84 base period. We also use the monthly gridded Argo temperature and salinity data (Roemmich and Gilson 2009; http://www.argo.ucsd.edu) to show the trend from 2005 through 2018. The data are on a 1° × 1° grid with 58 vertical pressure levels from the surface to 2000 m. The annual mean trend from 2005 to 2018 is calculated to represent the recent temperature and salinity changes in the Southern Ocean.

d. Latitude of mean ACC transport

Fixed sea surface height contours are often used to track ACC frontal displacements. This method is problematic because of large-scale steric expansion under global warming. To minimize the effect of steric expansion, we apply the method of Gille (2014) to find the latitude of mean ACC transport. Zonal ocean velocity at the surface (U_g) is related to the meridional gradient of sea surface height (SSH) through the geostrophic relationship:

$$U_g = -\frac{g}{f}\frac{\partial \mathrm{SSH}}{\partial y}, \tag{4}$$

where g is gravity, f is the Coriolis parameter, and y is the meridional length. The ACC fronts are expected to correspond to strong geostrophic velocities. Next, weighted by surface velocity, the mean latitude of the surface transport is computed as

$$\overline{\theta} = \frac{\int_{\theta_S}^{\theta_N} \theta U_g \, d\theta}{\int_{\theta_S}^{\theta_N} U_g \, d\theta}, \tag{5}$$

where $\overline{\theta}$ is the surface velocity weighted average latitude, θ_N and θ_S are the northern and southern integration limits of latitude, respectively, and U_g is zonal velocity calculated from Eq. (4). The mean latitude of the ACC is sensitive to the integration limits (Gille 2014), so we estimate uncertainty by conducting a Monte Carlo test with 1000 realizations, in which two integration limits are randomly perturbed using Gaussian random numbers with mean values at 40° and 60°S, respectively, and a standard deviation of 5° latitude.

We also use the independent method from Sen Gupta et al. (2009) and Meijers et al. (2012) to locate the position of the mean ACC, which is calculated at each longitude as the mean latitude within the latitude range defined by 50% of the maximum transport.

3. Southern Ocean temperature change

Buoy and Wstr under abrupt quadrupling of CO_2 create different zonal mean warming patterns in the Southern Ocean (Figs. 1c,d). For Buoy, the upper ocean temperature increases by around 3°C on the northern flank of the ACC and farther north (Fig. 1c). The warming decays with depth mainly along the climatological isopycnals (contours). South of the ACC, warming in the surface layer is weaker (by an average of 1.2°C between 60° and 75°S), likely due to continuous upwelling by the background ocean circulation of old deep water without a temperature anomaly (Armour et al. 2016). The ocean takes up heat where the deep water outcrops (Figs. 1a,c). The Ekman transport then advects the warmed water equatorward, where it is subducted and warms the thermocline between 20° and 50°S (Roemmich et al. 2015; Liu et al. 2018; Shi et al. 2018). The meridional gradient in temperature change across the ACC leads to greater

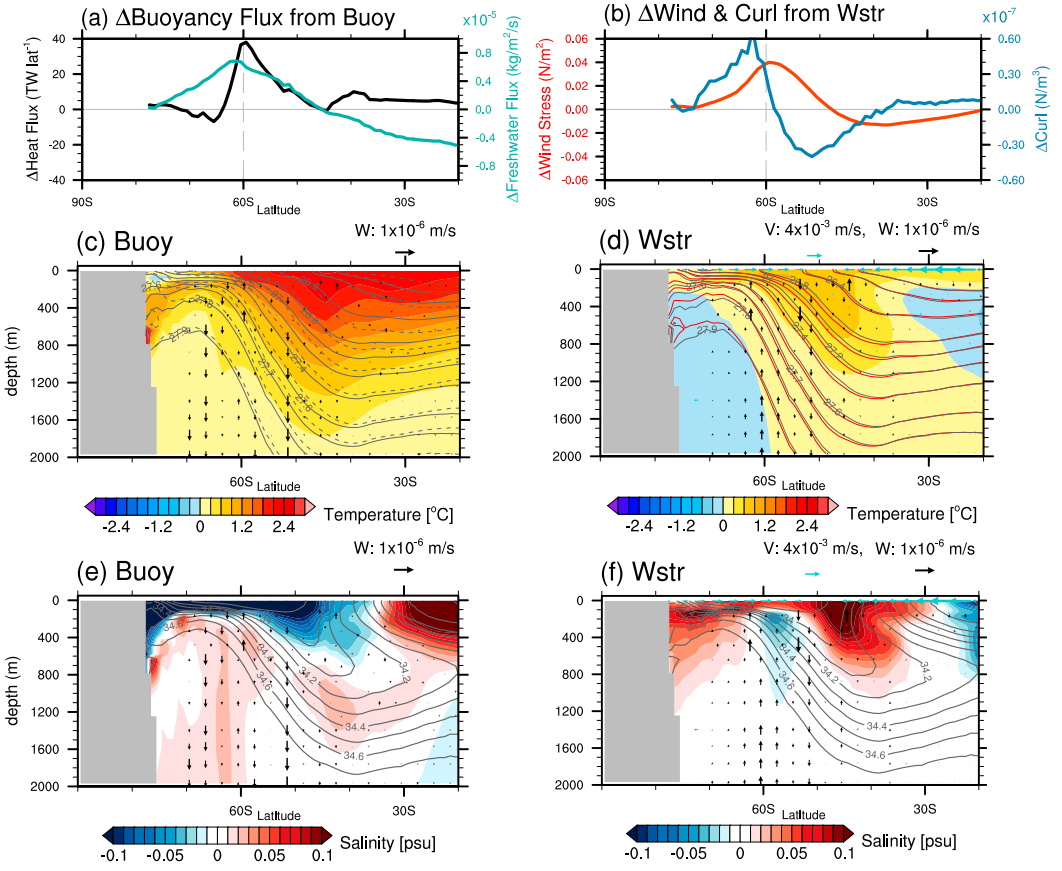

FIG. 1. Change of (a) zonally integrated surface heat flux (black) and zonal mean of precipitation minus evaporation (green) due to buoyancy forcing (Buoy) and (b) zonal mean of zonal wind stress (red) and wind stress curl (light blue) due to wind stress forcing (Wstr) over the Southern Ocean for CESM1, calculated as the average of years 41–90 minus the preindustrial control. The same averaging is used in subsequent figures unless otherwise specified. Zonal mean temperature change (shading) in the upper 2000 m in (c) Buoy and (d) Wstr for CESM1. Climatological isopycnals are shown as contours: dashed gray contours are from τ1w1c1, solid gray contours from τ1w1c4, and red contours from τ4w1c4. Zonal mean salinity change (shading) in the upper 2000 m for (e) Buoy and (f) Wstr, with climatological salinity profiles shown as contours. Vertical velocity and meridional surface velocity changes are shown as black and cyan vectors, respectively. All velocity variables include the eddy-induced velocity.

thermal-expansion-induced sea level rise in the north than in the south (Bouttes and Gregory 2014), resulting in enhanced zonal geostrophic velocity in the upper layer (Fig. 7b). We further discuss the important implications of this result in section 5.

Wind stress change (Wstr) also contributes to surface and subsurface warming between 40° and 55°S, with a maximum warming of over 1°C (Fig. 1d). Consistent with Fyfe et al. (2007), the wind forcing also induces subsurface cooling both south and north of the warmed region, a tripole pattern distinct from that of Buoy. This wind-driven subsurface temperature change is due to a combination of adiabatic and diabatic processes. The wind stress curl change is positive south of 58°S, negative within the ACC, and positive again but with small magnitude north of 35°S (Fig. 1b), leading to corresponding anomalous Ekman suction/pumping (Fig. 1d). At higher latitudes, the isopycnal displacements (contours in Fig. 1d) account for the warming and cooling patterns in different layers. The wind-forced, deepened isopycnals from 40° to 60°S enhance the subsurface warming that is due to Buoy (Fig. 1c). At lower latitudes, wind-forced, shoaling isopycnals are responsible for the cooling patch from 200 to 1000 m. The superposition of ocean vertical velocity change on climatological temperature illustrates this adiabatic heave process (Fig. S3a). Furthermore, the poleward shift and intensification of surface wind stress (red curve in Fig. 1b) leads to anomalous Ekman transport: enhanced equatorward Ekman transport at higher latitudes and reduced equatorward Ekman transport at lower latitudes (cyan vectors in Fig. 1d). Therefore, there is an ocean heat transport convergence in the surface layer in the vicinity of the ACC, which accounts for the surface warming induced by wind stress change. Meanwhile, the

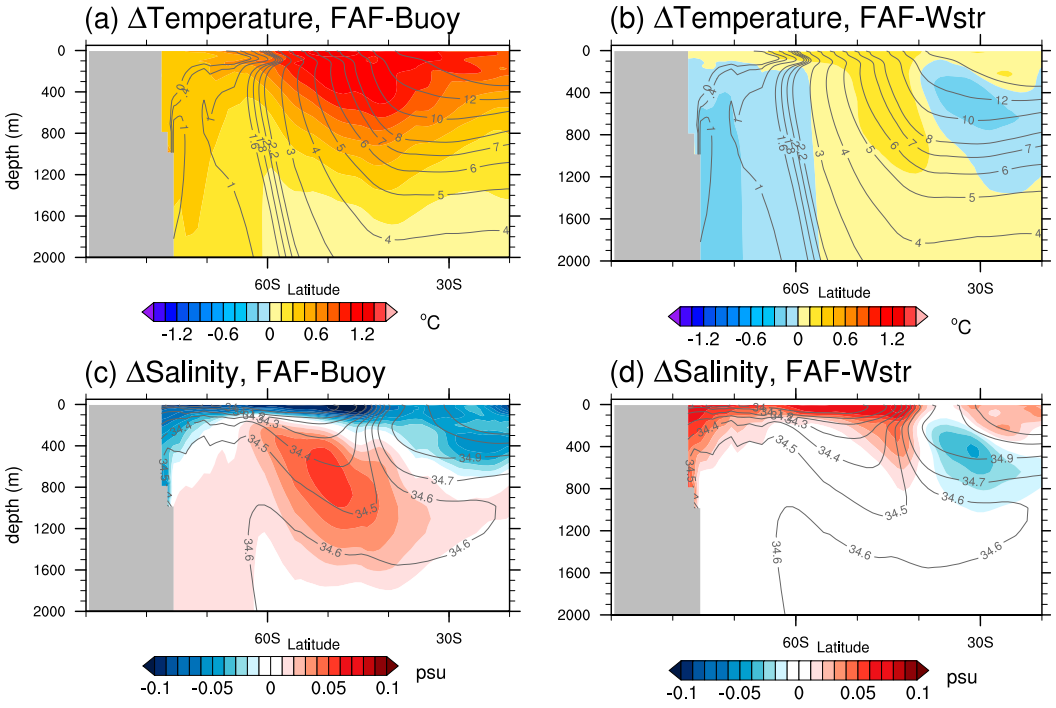

FIG. 2. Zonal mean temperature change in the upper 2000 m from the ensemble mean of FAFMIP experiments: (a) FAF-Buoy and (b) FAF-Wstr. (c),(d) As in (a) and (b), but showing corresponding zonal mean salinity change. The anomalies represent the difference between the 41–70-yr average and the climatology from the corresponding preindustrial control run. Contours show the 30-yr climatology.

wind-induced intensified residual MOC leads to a loss in surface heat flux around 45°S and a gain around 60°S (Liu et al. 2018). Within the ACC, the wind change reinforces the ocean warming due to Buoy. The wind-driven warming has a relatively small amplitude over the Southern Ocean compared with warming due to buoyancy forcing (Fig. S4): about one-fifth of Southern Ocean OHC change integrated between 30° and 90°S is driven by wind forcing (Fig. S4d). In fact, for the global ocean, most OHC change is found in Buoy (Fig. S4e), associated with ocean heat uptake.

The subsurface temperature change from FAFMIP experiments (Figs. 2a,b) is broadly consistent with the results from CESM1 (Figs. 1c,d), which confirms the fingerprints of change driven by Buoy and Wstr, respectively. Furthermore, different FAFMIP models also show similar warming patterns (Fig. S5). The observed subsurface warming in WOA and Argo is centered near 38°–42°S and is mainly located within the main thermocline layer (Figs. S6a,c), which is consistent with the model results (Fig. 1c). The weak subsurface cooling patch in observations between 400 and 1200 m and from 20°–30°S seems to be driven by wind stress change (Fig. 1d). For the surface temperature response, the observations show surface cooling at higher latitudes, especially regions south of the Subantarctic Front in the Pacific since the 1980s (Bindoff et al. 2013; Jones et al. 2013), which differs from the simulations. Although a number of studies have recently explored this difference between observed and simulated historical changes in the Southern Ocean (Bitz and Polvani 2012; Pauling et al. 2016; Kostov et al. 2017; Purich et al. 2018; Zhang et al. 2019; Rye et al. 2020; Haumann et al. 2020), the exact causes of this discrepancy are not fully understood.

4. Southern Ocean salinity and sea ice change

The Southern Ocean zonal mean salinity changes in the CESM partial-coupling experiments, driven by Buoy and Wstr, are shown in Fig. 1. For Buoy (Fig. 1e), the surface salinity change is dominated by strong surface freshening south of 35°S and strong surface salinification north of 35°S. The top panels of Fig. 3 show the 50-yr average salinity in the surface layer (0–50 m) for experiments τ1w1c1, τ1w1c4, and τ4w1c4. Freshening due to Buoy (Fig. 3d) is widespread in the Southern Ocean with the highest amplitudes in the Amundsen Sea, the Weddell Sea, and the Indian sector near the Antarctic coast. Moreover, the resemblance between zonal mean climatology (contours in Fig. 1e) and the salinity change due to buoyancy forcing (shading in Fig. 1e) indicates a strong global water cycle intensification under global

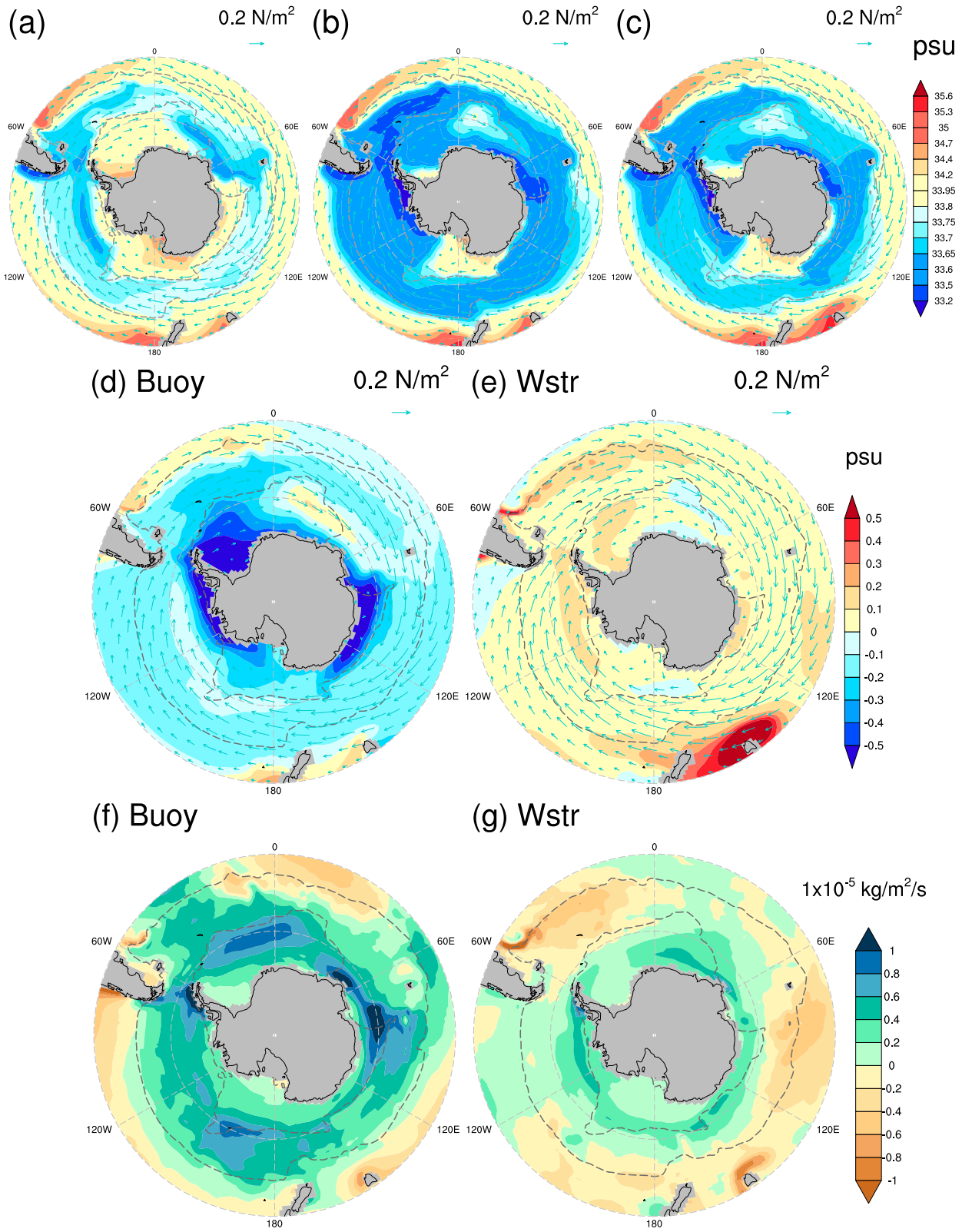

FIG. 3. Fifty-year climatological salinity within the upper 50 m for (a) τ1w1c1, (b) τ1w1c4, and (c) τ4w1c4 (see Table 1 for definitions). Change of salinity in the surface layer (0–50 m) in (d) Buoy and (e) Wstr. Change of precipitation minus evaporation over the Southern Ocean in (f) Buoy and (g) Wstr. The dashed gray contours indicate the northernmost and southernmost barotropic streamfunctions passing through the Drake Passage from preindustrial control, indicating the ACC envelope. Cyan vectors indicate climatological surface wind stress from preindustrial control.

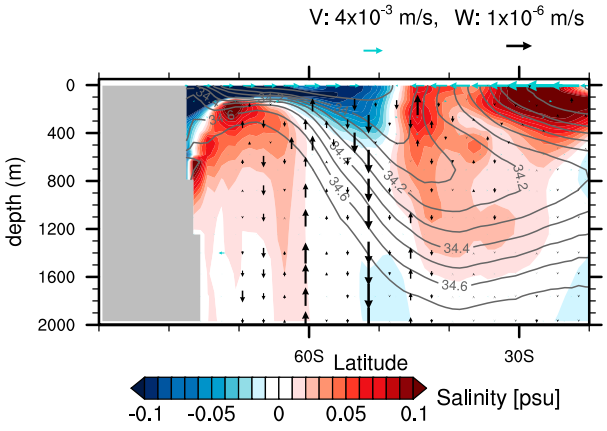

FIG. 4. Zonal mean salinity change (shading) in the upper 2000 m for Total. Climatological salinity profiles are shown as gray contours. Vertical velocity and meridional surface velocity changes are shown as black and cyan vectors, respectively.

warming: salinity decreases in precipitation-dominated (subpolar) regions and salinity increases in evaporation-dominated (subtropical) regions (green curve in Fig. 1a). However, in Buoy (Fig. 1e), the boundary between positive and negative salinity change (around 35°S) is much farther north than in previous observational and coupled model studies (Durack and Wijffels 2010; Böning et al. 2008; Swart et al. 2018), in which the boundary latitude is around 45°S (Figs. S6b,d). In the remainder of this section, we show that this boundary is mainly set by wind forcing since the combined results from Buoy and Wstr are in fact consistent with previous work.

The salinity change due to Wstr is dominated by salinification in the surface layer not only around the Antarctic coast but also in the vicinity of the ACC (Figs. 1f and 3e), which partially offsets the freshening driven by Buoy (Figs. 1e and 3d). Precipitation minus evaporation ($P - E$) increases at higher latitudes (Fig. 3g), which seems to be associated with a wind-induced sea ice coverage decrease (Fig. 5e), facilitating direct interaction between the atmosphere and ocean. Thus the increased Ekman upwelling, bringing saltier water from the deep ocean to the surface, overwhelms surface freshening due to increased freshwater flux from the atmosphere, leading to a surface layer salinity increase in the coastal region. The enhanced Ekman transport at higher latitudes (70°–55°S) then advects saltier water northward, leading to a salinity increase in the vicinity of the ACC. The decline of sea ice cover results in less freshwater flux from sea ice melt (Fig. 5e), which further increases surface salinity in the vicinity of the ACC. The weakened northward Ekman transport from 45° to 20°S also contributes to the surface salinity increase at midlatitudes. This wind-induced subsurface salinity change pattern is similar to that of temperature change (Fig. 1d), although the salinity change occurs in a shallower layer because the climatological salinity (Fig. S3b) is more stratified than the climatological temperature in the upper layer (Fig. S3a). In addition, at 40°S, salinity has a minimum at around 700 m (Antarctic Intermediate Water), so the wind-driven downward movements of isopycnals intensify the salinification above the minimum salinity layer and diminish salinification below. Therefore, pronounced salinity changes are shallower than the subsurface temperature changes. Hence we conclude that the mean stratification is critical for setting the warming and salinification patterns in the Southern Ocean.

For the zonal mean salinity change in the upper layer, the FAFMIP models show change consistent with CESM1: surface freshening due to Buoy and salinification due to Wstr (Figs. 2c,d). Maps of each model's salinity change in the upper 50 m also show the consistency in broadly distributed freshening due to buoyancy forcing and salinification due to wind forcing (Fig. S7). At intermediate depth from 40° to 60°S, all four FAF-Buoy runs (Fig. S8) and Buoy from CESM1 (Fig. 1e) show a salinity increase. In the FAFMIP models, buoyancy forcing can be further decomposed into a heat flux perturbation and a freshwater flux perturbation. The salinification at depth mostly results from surface heat uptake (Fig. S9c), which strongly increases stratification and restricts subduction of freshwater masses. Surface heat uptake contributes little to the surface salinity decrease, which is dominated by freshwater flux change (Fig. S9b). The heat uptake effect on salinity change shows large intermodel variation. For example, ACCESS-CM2 and MPI-ESM1.2-HR show very large salinification along the salinity minimum, while MIROC6, MRI-ESM2.0, and our CESM1 show a much weaker increase in salinity. The large intermodel spread may be related to biases in mean stratification of salinity, a topic that deserves further investigation. In addition, FAF-Buoy leads to freshening between 20° and 35°S in the upper layer (Fig. 2c), while salinification is found in the same region in Buoy (Fig. 1e). The result from Buoy is consistent with surface $P - E$ change (green curve in Fig. 1a), and surface $P - E$ change from FAF-Water (Fig. S9a) is consistent with results from Buoy, while it is still unclear how FAF-Water gives rise to a much broader freshening in the Southern Ocean.

For the total response to quadrupled CO_2, we linearly combine the results from Buoy and Wstr (Fig. 4). At higher latitudes, the surface layer is dominated by freshening due to more freshwater flux from the atmosphere (Figs. 3f,g), which overwhelms the upwelling of saltier water driven by wind. This can be attributed to the imposed strong CO_2 forcing ($4 \times CO_2$) which strongly warms the atmosphere. At midlatitudes (40°–50°), the salinity change is dominated by wind forcing. Overall, the combined response from Buoy and Wstr is broadly consistent with observed long-term surface

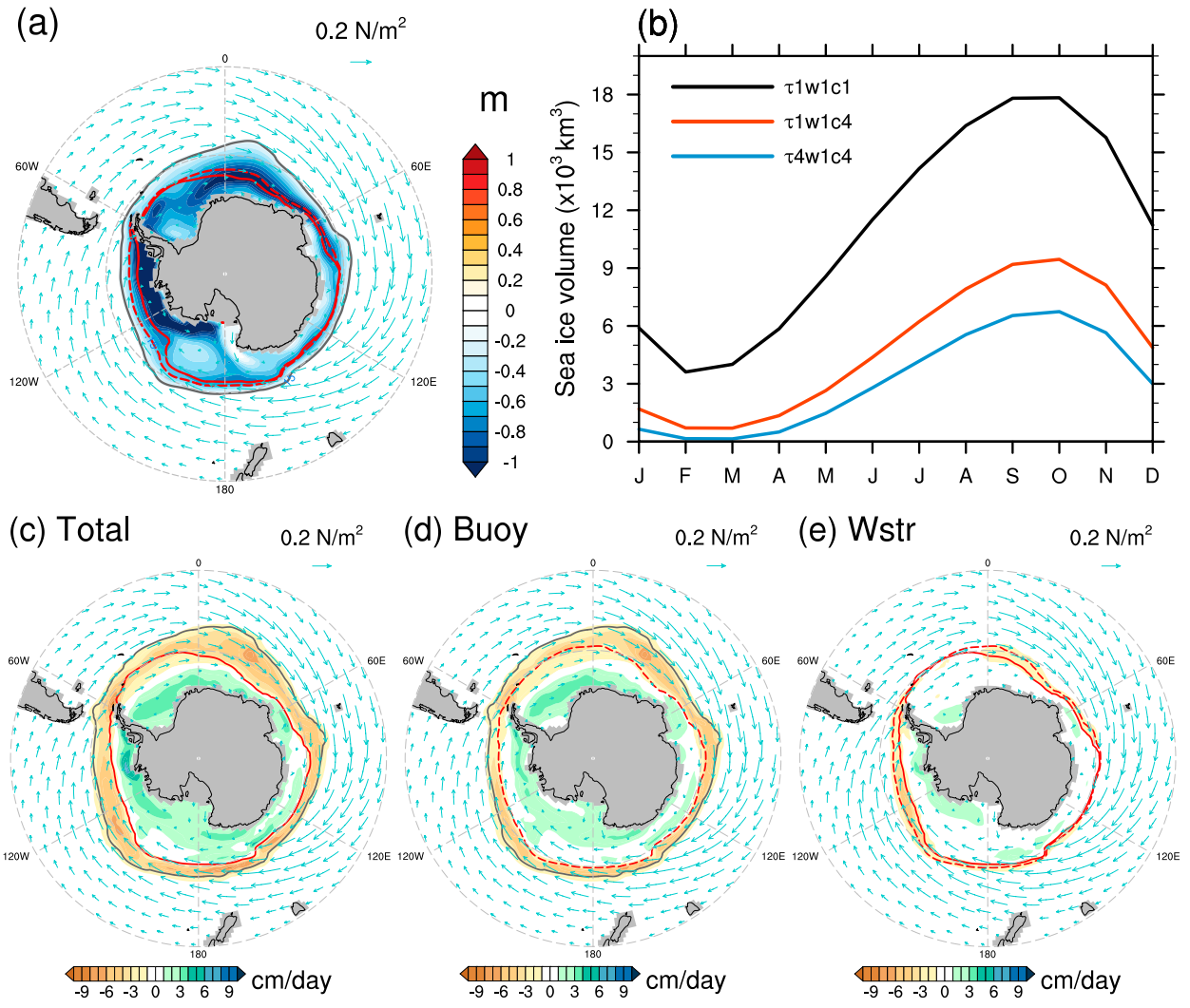

FIG. 5. (a) September sea ice thickness change in Total (shaded); sea ice edges (contours) based on 15% sea ice fraction from different experiments: τ1w1c1 (gray), τ1w1c4 (dashed red), and τ4w1c4 (solid red). (b) Annual cycle of sea ice volume in the Southern Hemisphere. Annual mean freshwater flux change from sea ice in response to (c) Total, (d) Buoy, and (e) Wstr. Positive values indicate more freshwater flux entering the ocean due to sea ice melting. Cyan vectors show climatological surface wind stress from τ1w1c1.

salinity change (Fig. S6) and previous studies (Durack and Wijffels 2010; Swart et al. 2018). A discrepancy at intermediate depths from 20° to 40°S appears to be associated with model drift due to prescribing surface wind stress since the fully coupled run ($4 \times CO_2 - CTRL$) shows a different pattern of salinity change (Fig. S1).

The atmospheric warming due to increased CO_2 in the partial-coupling experiments restricts sea ice formation such that the ice edge is farther south, especially in winter (Figs. 5a,b). Interestingly, the wind stress changes also lead to reduced sea ice coverage (solid red contour in Fig. 5a) because the enhanced vertical advection of heat driven by increased wind-driven upwelling results in SST increase (Figs. 6a,b) and sea ice retreat (Fig. 5a). Ferreira et al. (2015) show that the sea ice response to stratospheric ozone depletion depends on the time scale: the fast response is essentially confined to the mixed layer on short (~1 yr) time scales; the slow time-scale response (years to decades) is driven by ocean interior dynamics. The warming that we show 41–90 years after the CO_2 increase is the slow response. To isolate the fast response, we also show the change over the first two years (Figs. 6c,d). The sea ice retreat is small during winter (Fig. 6c), implying that the large seasonal sea ice cover dampens the wind effect on ocean circulation. In austral summer (Fig. 6d), the sea ice edge (15% of sea ice coverage) extends northward around the Weddell Sea and most of the coastal regions of East Antarctica. These fast responses are consistent with Purich et al. (2016), showing that during austral summer the enhanced

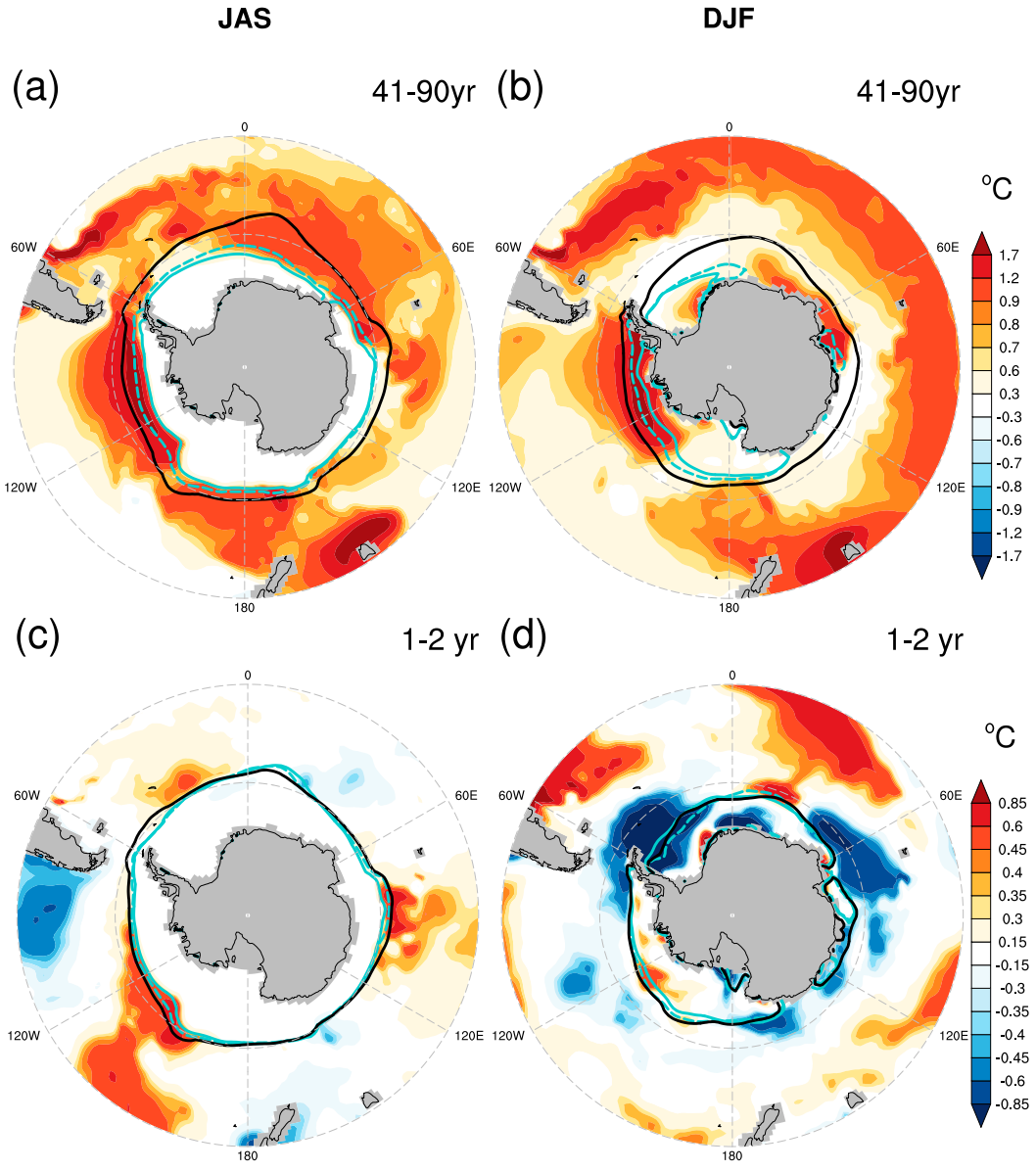

FIG. 6. Changes of SST (shading) and sea ice edge (contours) due to Wstr for different periods and seasons. Changes in years 41–90 relative to the control run for (a) JAS and (b) DJF. (c),(d) As in (a),(b), but for changes in the first two years. The black contour indicates the sea ice edge from τ1w1c1, the dashed cyan contour indicates sea ice edge when CO_2 is quadrupled without wind change (τ1w1c4), and the solid cyan contour indicates sea ice edge when both CO_2 and wind changes (τ4w1c4).

westerly wind leads to increased upwelling of cooler Winter Water just below the surface, which is conducive to increased sea ice coverage. As documented by Ferreira et al. (2015), the effects of wind on SST and sea ice extent are time dependent, leading to increased sea ice extent on short time scales but decreased sea ice extent in the longer term. The intensified wind can increase Antarctic sea ice extent through stronger equatorward Ekman transport, but this effect is overwhelmed gradually by enhanced upwelling of warmer, subsurface water. This nonmonotonic time evolution of Southern Ocean SST and sea ice extent driven by wind change, with the initial cooling (more sea ice extent) followed by long-term slow warming (less sea ice extent), is well discussed in previous research (Kostov et al. 2017; Holland et al. 2017; Seviour et al. 2016).

5. Antarctic Circumpolar Current response

We now quantify how buoyancy and wind effects contribute to ACC intensity and position. The major ACC

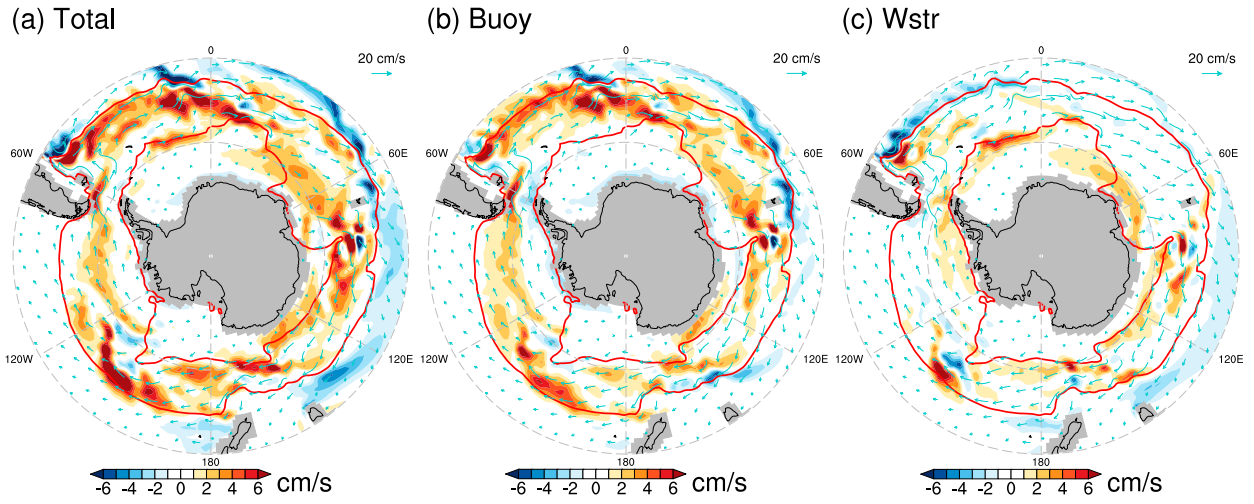

FIG. 7. Change of surface zonal geostrophic velocity U_g (shaded) for (a) Total, (b) Buoy, and (c) Wstr. Climatological ocean velocities in the surface layer (0–50 m) are shown as cyan vectors. The red contours show the ACC envelope. The velocity fields are shown in Fig. S10.

fronts coincide with strong geostrophic velocity U_g, which is calculated from sea surface height. Zonal geostrophic velocity changes are shown in Fig. 7. In Buoy, surface geostrophic velocity within the ACC strengthens on average by 1.25 cm s^{-1} (+15%). In the Atlantic and Indian sectors, this zonal velocity increase is stronger, which is in line with the zonal band of warming in the upper 2000 m north of the ACC (Fig. S4b). The meridional asymmetry of warming across the ACC results in asymmetric sea level rise through thermal expansion and hence increased zonal geostrophic velocity. Wind-induced change in surface zonal geostrophic velocity is positive overall (Wstr; Fig. 7c) but is patchy and weaker than the increase due to Buoy. The average velocity increase within the ACC is 0.52 cm s^{-1} (+6%). Interestingly, the surface horizontal circulation change within the ACC is dominated by buoyancy forcing.

The zonal mean patterns of zonal velocity change due to buoyancy and wind stress forcing changes for the whole water column are shown in Fig. 8. For Buoy, zonal velocity change is predominantly baroclinic, confined to the upper ocean (above 1500 m) (Fig. 8a), associated with density change across the ACC. Buoy increases the eastward ACC transport in the upper layer from 45° to 60°S and creates more westward transport from 35° to 45°S (Fig. 8a), consistent with maximum warming at 45°S (Fig. 1c). Freshening in the south and salinification in the north (Fig. 1e) would act to reduce the eastward ACC transport. Therefore, the spatial pattern of Southern Ocean heat uptake is responsible for the intensification of Buoy-driven circumpolar transport. In contrast, the wind stress-induced changes in the ACC have an equivalent barotropic structure, in which surface pressure is coherent with bottom pressure (Hughes et al. 2014). While it is vertically sheared, the zonal velocity increase due to wind stress penetrates to the ocean bottom (Fig. 8b). The excess wind-driven momentum is transferred downward by the eddy buoyancy flux and balanced by bottom form drag (Marshall et al. 2017). The FAFMIP results (Figs. 8c,d) agree with CESM1. FAF-Buoy leads to a weaker and shallower zonal velocity increase compared to Buoy from CESM1, which seems to be related to the relatively weaker warming (Fig. 2a) due to smaller external radiative forcing.

Whether the ACC shifts in latitude in response to increased atmospheric CO_2 is a commonly posed question, especially given the well-documented poleward shift of the westerly winds under warming (Gille 2008; Böning et al. 2008; Downes et al. 2011; Meijers et al. 2011; Kim and Orsi 2014; Gille 2014). We calculate the position of the ACC (Fig. 9) using two methods, from Gille (2014) and Meijers et al. (2012). Using the Gille (2014) method (Fig. 9a), Buoy accounts for a 0.3° southward shift of the mean ACC with a standard deviation of 0.9° as determined from 1000 Monte Carlo realizations. Similarly, Wstr accounts for a 0.3° southward shift with a standard deviation of 0.6°. In the Monte Carlo realizations, the northern and southern integration limits are randomly perturbed using Gaussian random numbers with a standard deviation of 5° latitude. The large range indicates the sensitivity of the mean ACC position to the choice of northern and southern integration limits in this method. Using the Meijers et al. (2012) method to calculate the ACC location (Fig. 9b), Buoy leads to a 0.3° ± 0.1° southward shift of ACC core and Wstr leads to a 0.4° ± 0.1° southward shift, with the uncertainty range here determined from temporal variability. Using this method, the ACC shifts due to both Buoy and Wstr are statistically significant at the 95% level. The

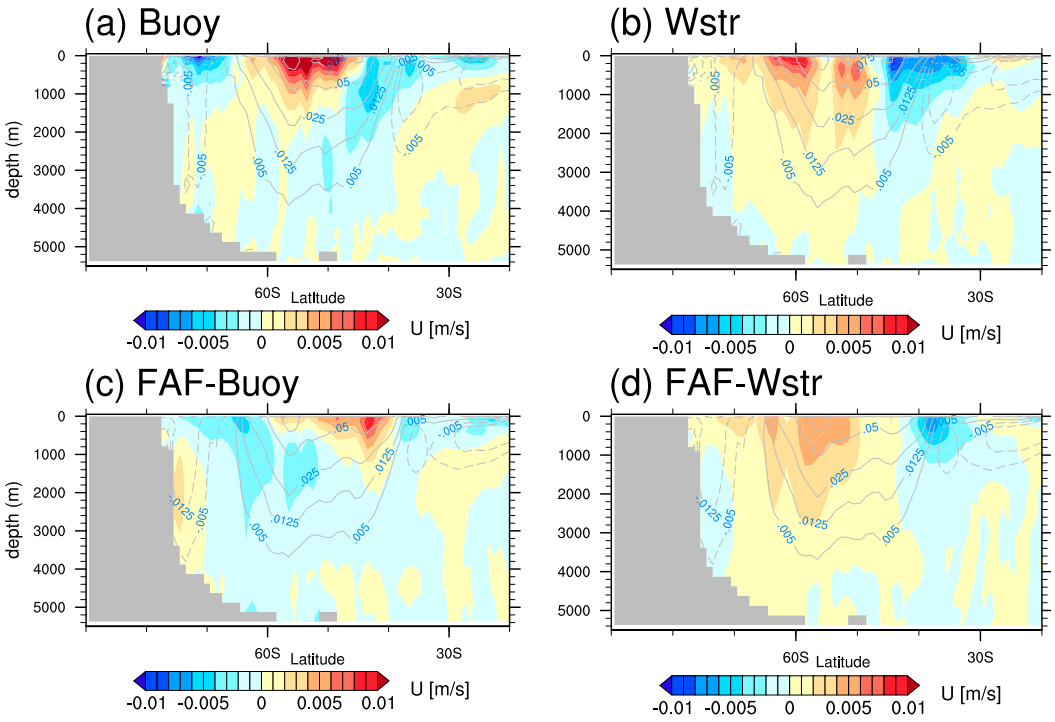

FIG. 8. Zonal mean of zonal velocity change in response to (a) Buoy and (b) Wstr from CEMS1 partial-coupling experiment and (c) FAF-Buoy and (d) FAF-Wstr from FAFMIP. The contours indicate zonal-mean climatology of zonal velocity from preindustrial control.

southward shift primarily takes place in the Atlantic and Indian sectors where surface fronts are strong. For comparison, the westerly wind position, based on the Gille (2014) method [substituting zonal wind stress for U_g in Eq. (5)], shifts southward by 1.2° ± 0.3° in latitude (Fig. 9c). All seasons show southward wind shifts, with maximum southward shift (2.1° ± 1.3°) in austral summer (December through February; not shown). This southward shift in annual mean wind is about 3 or 4 times greater than the southward shift in ACC position.

6. Discussion and conclusions

The Southern Ocean is regarded as a key player in the response of the global climate system to external forcing such as the anthropogenic emissions of CO_2. External CO_2 forcing gives rise to buoyancy flux change and surface wind stress change, which can lead to changes in ocean circulation and tracers. Previous studies largely focused on the response of the Southern Ocean to changes in westerly wind, whereas in this study we note that buoyancy forcing can play an even more critical role in Southern Ocean climate change. Using a novel partial coupling technique in CESM1, we separate the effects of buoyancy and wind (momentum) forcing on Southern Ocean temperature, salinity, and circulation changes under quadrupled CO_2. Since the external CO_2 forcing is large, buoyancy forcing dominates the Southern Ocean warming, with more warming on the northern than on the southern flank of the ACC due to the mean MOC. Buoyancy forcing also dominates surface freshening in the Southern Ocean. We find that the surface salinity increase over the Southern Ocean driven by wind forcing can substantially offset surface freshening driven by buoyancy forcing. Furthermore, buoyancy forcing leads to an increase in baroclinic transport within the ACC associated with an increase in the cross-stream density gradient. In contrast, wind stress change increases barotropic transport by altering the zonal momentum balance. Buoyancy forcing changes dominate the surface horizontal circulation acceleration.

About 80% of the total heat storage change to the south of 30°S from the quadrupling CO_2 case is attributed to buoyancy forcing, which includes the increase in the surface heat flux. The warming (cooling) pattern driven by wind forcing is associated with deepening (shoaling) of isopycnals. For salinity change, interestingly, buoyancy and wind forcing result in opposing changes, especially within the mixed layer. The surface freshening induced by buoyancy forcing is mainly attributed to more freshwater flux from the atmosphere, which is consistent with previous studies (e.g., Swart

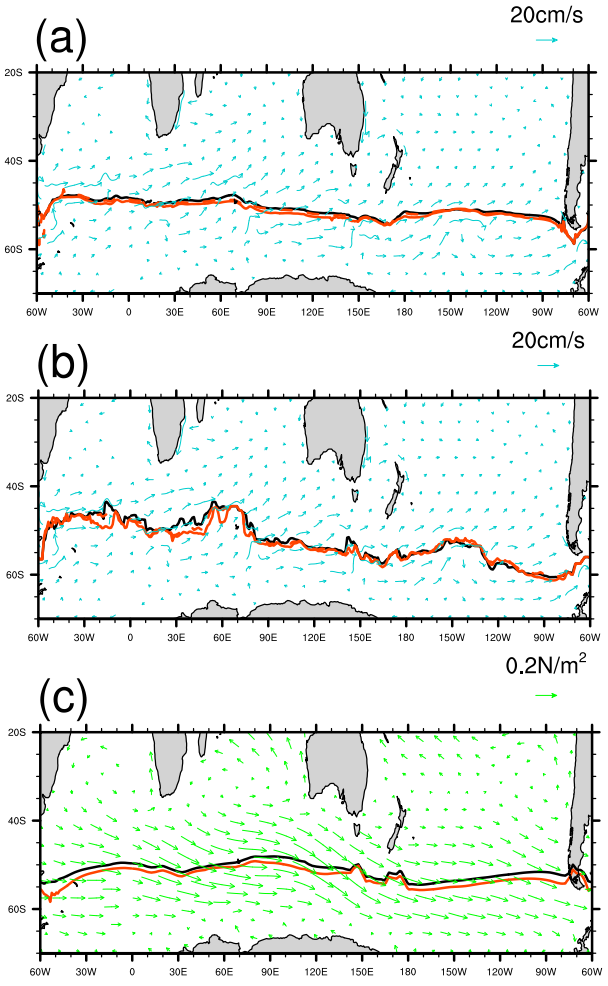

FIG. 9. (a) Positions of the mean ACC, based on the weighted mean zonal surface geostrophic velocity at each longitude. (b) Position of ACC core based on the method from Meijers et al. (2012). ACC position from τ1w1c1 (black), τ1w1c4 (dashed red), and τ4w1c4 (solid red). Climatological ocean velocity in the upper 50 m in the preindustrial control (cyan vectors). (c) As in (a), but showing positions of weighted mean center of zonal surface wind stress. Climatological surface wind stress from preindustrial control (green vectors).

et al. 2018). The wind stress change, however, leads to surface salinity increase, driven by increased Ekman upwelling of saltier deep water and northward Ekman advection. This wind-induced salinity increase offsets the freshening due to buoyancy forcing. At higher latitudes, the surface layer is dominated by buoyancy forcing, whereas at midlatitudes (40°–50°S), the salinity change is dominated by wind forcing. Hence the relative strength of buoyancy and wind forcing can significantly affect the pattern of salinity change. Accurate surface forcing is crucial to understanding the fingerprint of salinity change, in addition to the fingerprint of temperature change. Salinity change occurs at a shallower depth than temperature change, due to shallower stratification in mean salinity compared with temperature.

Buoyancy and wind forcing both trigger retreat of sea ice extent around the Antarctic, especially during austral winter when sea ice is formed (Fig. 5b). Thus, the northward advection of freshwater due to sea ice is reduced (Figs. 5c–e; Haumann et al. 2016; Abernathey et al. 2016). For wind forcing, the intensified upwelling of warmer subsurface water restricts the formation of sea ice, which overcompensates the equatorward extension of sea ice driven by intensified Ekman transport. Several modeling studies have shown that meltwater from the Antarctic ice sheet can cause significant global sea level rise, reduction of global mean atmospheric warming, and more stratified ocean surface water (de Lavergne et al. 2014; Fogwill et al. 2015; Bronselaer et al. 2018). Interestingly, even without an interactive ice sheet in our model (CESM1), we still find large-scale surface freshening driven by buoyancy forcing (Fig. 1e), which is consistent with results from Pauling et al. (2016). The observed SST cooling and expansion of Southern Ocean sea ice extent is reproduced by neither the idealized FAFMIP nor our CESM simulations, which seems to be a common issue in models. The poleward intensified westerly winds could lead to an initial surface cooling (Kostov et al. 2017; Holland et al. 2017), which would last only a few years. Surface freshening is also used in other studies to explain observed sea ice expansion, SST cooling, and subsurface warming, and is associated with a reduction of deep convection (Bintanja et al. 2013; de Lavergne et al. 2014; Purich et al. 2018). Bronselaer et al. (2020) and Rye et al. (2020) argue that Antarctic glacial melt is essential to recent Southern Ocean climate trends. However, some studies argue that the melting of the Antarctic ice sheet is too weak to trigger sea ice expansion (Swart and Fyfe 2013; Pauling et al. 2016; Haumann et al. 2020), and the enhanced northward freshwater transport by the sea ice is found to be the predominant cause of the recent observed trends in the high-latitude Southern Ocean (Haumann et al. 2020). Natural variability is also an important factor. For instance, Zhang et al. (2019) found that natural multidecadal variability in Southern Ocean convection may have strongly contributed to the observed temperature and sea ice trend. More work is required to explore the exact cause of the historical trends in the Southern Ocean and contribute to reliable future projections.

An increase in ACC transport that is weaker than expected given the increased winds in these experiments is consistent with recent studies (Morrison and Hogg 2013; Dufour et al. 2012; Farneti et al. 2015; Langlais et al. 2015). For example, in Bishop et al.'s (2016) high-resolution ocean model, a 41% increase in zonal wind

stress led to only about a 6% increase in ACC transport; the weakness of the transport response was attributed to eddy saturation due to stronger baroclinicity and instability in the ACC. In our Wstr experiment, we find a 5% (8.7 ± 2.3 Sv) increase in Drake Passage transport in response to a 19% increase in westerly winds ($+0.036\,N\,m^{-2}$), supporting the eddy saturation hypothesis. (Here the uncertainty denotes interannual variability.) Hogg (2010) and Stössel et al. (2015) point out that the strength of mean ACC strongly depends on the surface buoyancy flux. In our study, we find that buoyancy forcing causes a positive but weaker Drake Passage transport change (3.1 ± 1.6 Sv) by increasing the meridional density gradient due to stronger warming on the northern flank of the ACC than to the south. More importantly, we find that wind and buoyancy forcing lead to different vertical structures of ACC transport change. While previous research has focused on the effect of wind on ACC change, we find that the surface horizontal current acceleration within the ACC is dominated by buoyancy forcing, rather than change in wind. We show that wind changes create a more barotropic increase in circumpolar transport, manifested as an intensified zonal circumpolar current from the surface to the bottom. For buoyancy forcing, ACC strength is mainly governed by changes in the density structure, in other words, by the baroclinic thermal wind transport. Farneti et al. (2015) evaluate the Drake Passage transport change due to wind forcing and buoyancy forcing for 1958–2007 in a suite of cases from the second phase of the Coordinated Ocean-Ice Reference Experiments (CORE-II). They find that wind forcing dominates the increase in transport despite eddy saturation. Buoyancy forcing in their experiments, however, leads to a weak reduction in transport, which is inconsistent with our results. They attribute this reduction in transport to a flattening of the isopycnals. We also find flattening of isopycnals in Buoy (Fig. 1c). However, the surface pressure gradient force from 45° to 60°S increases in our experiments due to the asymmetric warming across the ACC, hence leading to a zonal transport increase in the upper layer (Fig. 7a). One possible explanation for the discrepancy is that Farneti et al.'s (2015) global mean surface heat flux during their recent five decades is $2.63\,W\,m^{-2}$, which is much smaller than in our 4 × CO_2 experiment ($6.25\,W\,m^{-2}$ for the first 10-yr average), so the ACC response to the meridional gradient of warming is not significant in their simulations. As a caveat, the resolution of our model is not fine enough to resolve mesoscale eddies, so the results shown here are based on eddy parameterization. Future investigations should consider how eddy resolution contributes to Southern Ocean responses to buoyancy and wind forcing.

Estimates of the shift in the ACC position can be biased if based on fixed SSH contours, which are strongly affected by large-scale steric expansion associated with warming and freshening of the Southern Ocean. By using two independent methods from Gille (2014) and Meijers et al. (2012), associated with meridional gradient of SSH or streamfunction, we show that Buoy and Wstr each result in 0.3° ± 0.1° southward shifts. The significance of the shift is based on the method from Meijers et al. (2012). The small southward shift from Buoy and Wstr may be associated with the shift of the Subtropical Front north of the ACC, which is strongly surface intensified and confined in the upper layer (Graham et al. 2012). In addition, we find that the southward shifts of the mean ACC mainly occur in the eastern Atlantic and Indian sectors where the fronts are strongest.

We diagnosed the distinct patterns of Southern Ocean change driven by buoyancy and wind forcing only due to an unrealistically strong anthropogenic forcing. The 4 × CO_2 forcing (around $7\,W\,m^{-2}$) in our experiments is much stronger than the actual well-mixed GHG radiative forcing ($2.83 \pm 0.29\,W\,m^{-2}$) in 2011 relative to 1750 (Myhre et al. 2013), and is comparable to the radiative forcing ($8.5\,W\,m^{-2}$) from representative concentration pathway (RCP) 8.5 in the year 2100. The wind stress change ($+0.036\,N\,m^{-2}$) in our simulation is a little smaller than that in RCP8.5, at $0.047\,N\,m^{-2}$ (2080–2100 anomaly relative to the piControl runs from the ensemble mean of 27 CMIP5 models). Even so, the fingerprint of change due to the separate effects of buoyancy and wind forcing can help us better understand the long-term change in the Southern Ocean. In reality, stratospheric ozone depletion, which is not considered in our study, can also give rise to poleward-intensified westerlies (Thompson 2002). In the future, the relative strength and importance of buoyancy and wind forcing are likely to change due to the recovery of stratospheric ozone, which can weaken the westerlies. Reduction in anthropogenic aerosols might intensify the westerlies (e.g., Shi et al. 2018). Therefore, the Southern Ocean responses are likely to evolve with changes in these forcing terms. For instance, since we find that surface salinity change is determined by the compensation between buoyancy and wind forcing effects, we would expect a distinct salinity change pattern in the future relative to the historical change as the relative strength of buoyancy and wind forcing evolves.

Acknowledgments. J.-R. Shi is supported by U.S. National Science Foundation (AGS-1637450) and the Southern Ocean Carbon and Climate Observations and Modeling project (SOCCOM) under National Science Foundation Award (PLR-1425989). L.D.T. and S.T.G. are also supported by SOCCOM, and S.T.G. received additional support from NSF Award OCE-1658001. W.L. is supported by the Regents' Faculty Fellowship, and also

by the Alfred P. Sloan Foundation as a Research Fellow. We thank the CMIP6 groups and the FAFMIP group for producing and making available their model output, which is available from https://esgf-node.llnl.gov/projects/cmip6/. The Argo data used here were collected and made freely available by the International Argo Program and by the national programs that contribute to it (http://argo.ucsd.edu). The World Ocean Atlas 2018 products are available on the NOAA National Oceanographic Data Center website (https://www.nodc.noaa.gov/OC5/woa18/).

REFERENCES

Abernathey, R. P., I. Cerovecki, P. R. Holland, E. Newsom, M. Mazloff, and L. D. Talley, 2016: Water-mass transformation by sea ice in the upper branch of the Southern Ocean overturning. *Nat. Geosci.*, **9**, 596–601, https://doi.org/10.1038/ngeo2749.

Armour, K. C., J. Marshall, J. R. Scott, A. Donohoe, and E. R. Newsom, 2016: Southern Ocean warming delayed by circumpolar upwelling and equatorward transport. *Nat. Geosci.*, **9**, 549–554, https://doi.org/10.1038/ngeo2731.

Beadling, R. L., J. L. Russell, R. J. Stouffer, P. J. Goodman, and M. Mazloff, 2019: Assessing the quality of Southern Ocean circulation in CMIP5 AOGCM and Earth system model simulations. *J. Climate*, **32**, 5915–5940, https://doi.org/10.1175/JCLI-D-19-0263.1.

Bindoff, N. L., and Coauthors, 2013: Detection and attribution of climate change: From global to regional. *Climate Change 2013: The Physical Science Basis*, T. F. Stocker et al., Eds., Cambridge University Press, 867–952.

Bintanja, R., G. J. Van Oldenborgh, S. S. Drijfhout, B. Wouters, and C. A. Katsman, 2013: Important role for ocean warming and increased ice-shelf melt in Antarctic sea-ice expansion. *Nat. Geosci.*, **6**, 376–379, https://doi.org/10.1038/ngeo1767.

Bishop, S. P., P. R. Gent, F. O. Bryan, A. F. Thompson, M. C. Long, and R. Abernathey, 2016: Southern Ocean overturning compensation in an eddy-resolving climate simulation. *J. Phys. Oceanogr.*, **46**, 1575–1592, https://doi.org/10.1175/JPO-D-15-0177.1.

Bitz, C. M., and L. M. Polvani, 2012: Antarctic climate response to stratospheric ozone depletion in a fine resolution ocean climate model. *Geophys. Res. Lett.*, **39**, L20705, https://doi.org/10.1029/2012GL053393.

Böning, C. W., A. Dispert, M. Visbeck, S. R. Rintoul, and F. U. Schwarzkopf, 2008: The response of the Antarctic Circumpolar Current to recent climate change. *Nat. Geosci.*, **1**, 864–869, https://doi.org/10.1038/ngeo362.

Bouttes, N., and J. M. Gregory, 2014: Attribution of the spatial pattern of CO_2-forced sea level change to ocean surface flux changes. *Environ. Res. Lett.*, **9**, 034004, https://doi.org/10.1088/1748-9326/9/3/034004.

Bracegirdle, T. J., P. Hyder, and C. R. Holmes, 2018: CMIP5 diversity in southern westerly jet projections related to historical sea ice area: Strong link to strengthening and weak link to shift. *J. Climate*, **31**, 195–211, https://doi.org/10.1175/JCLI-D-17-0320.1.

Bronselaer, B., M. Winton, S. M. Griffies, W. J. Hurlin, K. B. Rodgers, O. V. Sergienko, R. J. Stouffer, and J. L. Russell, 2018: Change in future climate due to Antarctic meltwater. *Nature*, **564**, 53–58, https://doi.org/10.1038/s41586-018-0712-z.

——, and Coauthors, 2020: Importance of wind and meltwater for observed chemical and physical changes in the Southern Ocean. *Nat. Geosci.*, **13**, 35–42, https://doi.org/10.1038/s41561-019-0502-8.

Cheng, L., and J. Zhu, 2016: Benefits of CMIP5 multimodel ensemble in reconstructing historical ocean subsurface temperature variations. *J. Climate*, **29**, 5393–5416, https://doi.org/10.1175/JCLI-D-15-0730.1.

——, K. E. Trenberth, M. D. Palmer, J. Zhu, and J. P. Abraham, 2016: Observed and simulated full-depth ocean heat-content changes for 1970–2005. *Ocean Sci.*, **12**, 925–935, https://doi.org/10.5194/os-12-925-2016.

de Lavergne, C., J. B. Palter, E. D. Galbraith, R. Bernardello, and I. Marinov, 2014: Cessation of deep convection in the open Southern Ocean under anthropogenic climate change. *Nat. Climate Change*, **4**, 278–282, https://doi.org/10.1038/nclimate2132.

Desbruyères, D. G., S. G. Purkey, E. L. McDonagh, G. C. Johnson, and B. A. King, 2016: Deep and abyssal ocean warming from 35 years of repeat hydrography. *Geophys. Res. Lett.*, **43**, 10 356–10 365, https://doi.org/10.1002/2016GL070413.

Donohue, K. A., K. L. Tracey, D. R. Watts, M. P. Chidichimo, and T. K. Chereskin, 2016: Mean Antarctic Circumpolar Current transport measured in Drake Passage. *Geophys. Res. Lett.*, **43**, 11 760–11 767, https://doi.org/10.1002/2016GL070319.

Downes, S. M., A. S. Budnick, J. L. Sarmiento, and R. Farneti, 2011: Impacts of wind stress on the Antarctic Circumpolar Current fronts and associated subduction. *Geophys. Res. Lett.*, **38**, L11605, https://doi.org/10.1029/2011GL047668.

Dufour, C. O., J. Le Sommer, J. D. Zika, M. Gehlen, J. C. Orr, P. Mathiot, and B. Barnier, 2012: Standing and transient eddies in the response of the Southern Ocean meridional overturning to the southern annular mode. *J. Climate*, **25**, 6958–6974, https://doi.org/10.1175/JCLI-D-11-00309.1.

Durack, P. J., and S. E. Wijffels, 2010: Fifty-year trends in global ocean salinities and their relationship to broad-scale warming. *J. Climate*, **23**, 4342–4362, https://doi.org/10.1175/2010JCLI3377.1.

——, ——, and R. J. Matear, 2012: Ocean salinities reveal strong global water cycle intensification during 1950 to 2000. *Science*, **336**, 455–458, https://doi.org/10.1126/science.1212222.

Farneti, R., T. L. Delworth, A. J. Rosati, S. M. Griffies, and F. Zeng, 2010: The role of mesoscale eddies in the rectification of the Southern Ocean response to climate change. *J. Phys. Oceanogr.*, **40**, 1539–1557, https://doi.org/10.1175/2010JPO4353.1.

——, and Coauthors, 2015: An assessment of Antarctic Circumpolar Current and Southern Ocean meridional overturning circulation during 1958–2007 in a suite of interannual CORE-II simulations. *Ocean Modell.*, **93**, 84–120, https://doi.org/10.1016/j.ocemod.2015.07.009.

Ferreira, D., J. Marshall, C. M. Bitz, S. Solomon, and A. Plumb, 2015: Antarctic Ocean and sea ice response to ozone depletion: A two-time-scale problem. *J. Climate*, **28**, 1206–1226, https://doi.org/10.1175/JCLI-D-14-00313.1.

Fogwill, C. J., S. J. Phipps, C. S. M. Turney, and N. R. Golledge, 2015: Sensitivity of the Southern Ocean to enhanced regional Antarctic ice sheet meltwater input. *Earth's Future*, **3**, 317–329, https://doi.org/10.1002/2015EF000306.

Frölicher, T. L., J. L. Sarmiento, D. J. Paynter, J. P. Dunne, J. P. Krasting, and M. Winton, 2015: Dominance of the Southern Ocean in anthropogenic carbon and heat uptake in CMIP5 models. *J. Climate*, **28**, 862–886, https://doi.org/10.1175/JCLI-D-14-00117.1.

Fyfe, J. C., and O. A. Saenko, 2006: Simulated changes in the extratropical Southern Hemisphere winds and currents. *Geophys. Res. Lett.*, **33**, L06701, https://doi.org/10.1029/2005GL025332.

——, ——, K. Zickfeld, M. Eby, and A. J. Weaver, 2007: The role of poleward-intensifying winds on Southern Ocean warming. *J. Climate*, **20**, 5391–5400, https://doi.org/10.1175/2007JCLI1764.1.

Gent, P. R., 2016: Effects of Southern Hemisphere wind changes on the meridional overturning circulation in ocean models. *Annu. Rev. Mar. Sci.*, **8**, 79–94, https://doi.org/10.1146/annurev-marine-122414-033929.

——, and J. C. McWilliams, 1990: Isopycnal mixing in ocean circulation models. *J. Phys. Oceanogr.*, **20**, 150–155, https://doi.org/10.1175/1520-0485(1990)020<0150:IMIOCM>2.0.CO;2.

Gille, S. T., 2002: Warming of the Southern Ocean since the 1950s. *Science*, **295**, 1275–1277, https://doi.org/10.1126/science.1065863.

——, 2008: Decadal-scale temperature trends in the Southern Hemisphere ocean. *J. Climate*, **21**, 4749–4765, https://doi.org/10.1175/2008JCLI2131.1.

——, 2014: Meridional displacement of the Antarctic Circumpolar Current. *Philos. Trans. Roy. Soc. London*, **A372**, 20130273, https://doi.org/10.1098/rsta.2013.0273.

Gillett, N. P., 2003: Simulation of recent Southern Hemisphere climate change. *Science*, **302**, 273–275, https://doi.org/10.1126/science.1087440.

Graham, R. M., A. M. De Boer, K. J. Heywood, M. R. Chapman, and D. P. Stevens, 2012: Southern Ocean fronts: Controlled by wind or topography? *J. Geophys. Res.*, **117**, C08018, https://doi.org/10.1029/2012JC007887.

Gregory, J. M., and Coauthors, 2016: The Flux-Anomaly-Forced Model Intercomparison Project (FAFMIP) contribution to CMIP6: Investigation of sea-level and ocean climate change in response to CO_2 forcing. *Geosci. Model Dev.*, **9**, 3993–4017, https://doi.org/10.5194/gmd-9-3993-2016.

Gutjahr, O., D. Putrasahan, K. Lohmann, J. H. Jungclaus, J. S. Von Storch, N. Brüggemann, H. Haak, and A. Stössel, 2019: Max Planck Institute Earth System Model (MPI-ESM1.2) for the High-Resolution Model Intercomparison Project (HighResMIP). *Geosci. Model Dev.*, **12**, 3241–3281, https://doi.org/10.5194/gmd-12-3241-2019.

Hallberg, R., and A. Gnanadesikan, 2006: The role of eddies in determining the structure and response of the wind-driven Southern Hemisphere overturning: Results from the Modeling Eddies in the Southern Ocean (MESO) Project. *J. Phys. Oceanogr.*, **36**, 2232–2252, https://doi.org/10.1175/JPO2980.1.

Haumann, F. A., N. Gruber, M. Münnich, I. Frenger, and S. Kern, 2016: Sea-ice transport driving Southern Ocean salinity and its recent trends. *Nature*, **537**, 89–92, https://doi.org/10.1038/nature19101.

——, ——, and ——, 2020: Sea-ice induced Southern Ocean subsurface warming and surface cooling in a warming climate. *AGU Adv.*, **1**, e2019AV000132, https://doi.org/10.1029/2019av000132.

Helm, K. P., N. L. Bindoff, and J. A. Church, 2010: Changes in the global hydrological-cycle inferred from ocean salinity. *Geophys. Res. Lett.*, **37**, L18701, https://doi.org/10.1029/2010GL044222.

Hirst, T., D. Bi, H. Yan, S. Marsland, M. Dix, and A. Sullivan, 2015: The ACCESS-CM2 coupled climate model—Status and plans including contribution to CMIP6. CSIRO, http://hdl.handle.net/102.100.100/91600?index=1.

Hogg, A. M., 2010: An Antarctic Circumpolar Current driven by surface buoyancy forcing. *Geophys. Res. Lett.*, **37**, L23601, https://doi.org/10.1029/2010GL044777.

Holland, M. M., L. Landrum, Y. Kostov, and J. Marshall, 2017: Sensitivity of Antarctic sea ice to the Southern Annular Mode in coupled climate models. *Climate Dyn.*, **49**, 1813–1831, https://doi.org/10.1007/s00382-016-3424-9.

Hughes, C. W., J. Williams, A. C. Coward, and B. A. de Cuevas, 2014: Antarctic circumpolar transport and the southern mode: A model investigation of interannual to decadal timescales. *Ocean Sci.*, **10**, 215–225, https://doi.org/10.5194/os-10-215-2014.

Hurrell, J. W., and Coauthors, 2013: The Community Earth System Model: A framework for collaborative research. *Bull. Amer. Meteor. Soc.*, **94**, 1339–1360, https://doi.org/10.1175/BAMS-D-12-00121.1.

Jacobs, S. S., 2002: Freshening of the Ross Sea during the late 20th century. *Science*, **297**, 386–389, https://doi.org/10.1126/science.1069574.

Jones, G. S., P. A. Stott, and N. Christidis, 2013: Attribution of observed historical near-surface temperature variations to anthropogenic and natural causes using CMIP5 simulations. *J. Geophys. Res. Atmos.*, **118**, 4001–4024, https://doi.org/10.1002/JGRD.50239.

Kay, J. E., and Coauthors, 2015: The Community Earth System Model (CESM) large ensemble project: A community resource for studying climate change in the presence of internal climate variability. *Bull. Amer. Meteor. Soc.*, **96**, 1333–1349, https://doi.org/10.1175/BAMS-D-13-00255.1.

——, C. Wall, V. Yettella, B. Medeiros, C. Hannay, P. Caldwell, and C. Bitz, 2016: Global climate impacts of fixing the Southern Ocean shortwave radiation bias in the Community Earth System Model (CESM). *J. Climate*, **29**, 4617–4636, https://doi.org/10.1175/JCLI-D-15-0358.1.

Kim, Y. S., and A. H. Orsi, 2014: On the variability of Antarctic Circumpolar Current fronts inferred from 1992–2011 altimetry. *J. Phys. Oceanogr.*, **44**, 3054–3071, https://doi.org/10.1175/JPO-D-13-0217.1.

Kostov, Y., J. Marshall, U. Hausmann, K. C. Armour, D. Ferreira, and M. M. Holland, 2017: Fast and slow responses of Southern Ocean sea surface temperature to SAM in coupled climate models. *Climate Dyn.*, **48**, 1595–1609, https://doi.org/10.1007/s00382-016-3162-z.

Langlais, C. E., S. R. Rintoul, and J. D. Zika, 2015: Sensitivity of Antarctic Circumpolar Current transport and eddy activity to wind patterns in the Southern Ocean. *J. Phys. Oceanogr.*, **45**, 1051–1067, https://doi.org/10.1175/JPO-D-14-0053.1.

Large, W. G., J. C. McWilliams, and S. C. Doney, 1994: Oceanic vertical mixing: A review and a model with a nonlocal boundary layer parameterization. *Rev. Geophys.*, **32**, 363–403, https://doi.org/10.1029/94RG01872.

Lee, S., and S. B. Feldstein, 2013: Detecting ozone- and greenhouse gas–driven wind trends with observational data. *Science*, **339**, 563–567, https://doi.org/10.1126/science.1225154.

Liu, W., J. Lu, and S.-P. Xie, 2015: Understanding the Indian Ocean response to double CO_2 forcing in a coupled model. *Ocean Dyn.*, **65**, 1037–1046, https://doi.org/10.1007/s10236-015-0854-6.

——, ——, ——, and A. Fedorov, 2018: Southern Ocean heat uptake, redistribution, and storage in a warming climate: The role of meridional overturning circulation. *J. Climate*, **31**, 4727–4743, https://doi.org/10.1175/JCLI-D-17-0761.1.

Lu, J., and B. Zhao, 2012: The role of oceanic feedback in the climate response to doubling CO_2. *J. Climate*, **25**, 7544–7563, https://doi.org/10.1175/JCLI-D-11-00712.1.

Manabe, S., K. Bryan, and M. J. Spelman, 1990: Transient response of a global ocean–atmosphere model to a doubling of atmospheric carbon dioxide. *J. Phys. Oceanogr.*, **20**, 722–749, https://doi.org/10.1175/1520-0485(1990)020<0722:TROAGO>2.0.CO;2.

Marshall, D. P., M. H. P. Ambaum, J. R. Maddison, D. R. Munday, and L. Novak, 2017: Eddy saturation and frictional control of the Antarctic Circumpolar Current. *Geophys. Res. Lett.*, **44**, 286–292, https://doi.org/10.1002/2016GL071702.

Marshall, G. J., 2003: Trends in the southern annular mode from observations and reanalyses. *J. Climate*, **16**, 4134–4143, https://doi.org/10.1175/1520-0442(2003)016<4134:TITSAM>2.0.CO;2.

Meijers, A. J. S., N. L. Bindoff, and S. R. Rintoul, 2011: Frontal movements and property fluxes: Contributions to heat and

freshwater trends in the Southern Ocean. *J. Geophys. Res.*, **116**, C08024, https://doi.org/10.1029/2010JC006832.

——, E. Shuckburgh, N. Bruneau, J. B. Sallee, T. J. Bracegirdle, and Z. Wang, 2012: Representation of the Antarctic Circumpolar Current in the CMIP5 climate models and future changes under warming scenarios. *J. Geophys. Res.*, **117**, C12008, https://doi.org/10.1029/2012JC008412.

Meredith, M. P., and A. M. Hogg, 2006: Circumpolar response of Southern Ocean eddy activity to a change in the southern annular mode. *Geophys. Res. Lett.*, **33**, L16608, https://doi.org/10.1029/2006GL026499.

——, A. C. Naveira Garabato, A. M. Hogg, and R. Farneti, 2012: Sensitivity of the overturning circulation in the Southern Ocean to decadal changes in wind forcing. *J. Climate*, **25**, 99–110, https://doi.org/10.1175/2011JCLI4204.1.

Morrison, A. K., and A. M. Hogg, 2013: On the relationship between Southern Ocean overturning and ACC transport. *J. Phys. Oceanogr.*, **43**, 140–148, https://doi.org/10.1175/JPO-D-12-057.1.

——, S. M. Griffies, M. Winton, W. G. Anderson, and J. L. Sarmiento, 2016: Mechanisms of Southern Ocean heat uptake and transport in a global eddying climate model. *J. Climate*, **29**, 2059–2075, https://doi.org/10.1175/JCLI-D-15-0579.1.

Myhre, G., and Coauthors, 2013: Anthropogenic and natural radiative forcing. *Climate Change 2013: The Physical Science Basis*, T. F. Stocker et al., Eds., Cambridge University Press, 659–740, https://doi.org/10.1017/CBO9781107415324.018.

Paolo, F. S., H. A. Fricker, and L. Padman, 2015: Volume loss from Antarctic ice shelves is accelerating. *Science*, **348**, 327–331, https://doi.org/10.1126/science.aaa0940.

Pauling, A. G., C. M. Bitz, I. J. Smith, and P. J. Langhorne, 2016: The response of the Southern Ocean and Antarctic sea ice to freshwater from ice shelves in an Earth system model. *J. Climate*, **29**, 1655–1672, https://doi.org/10.1175/JCLI-D-15-0501.1.

Purich, A., W. Cai, M. H. England, and T. Cowan, 2016: Evidence for link between modelled trends in Antarctic sea ice and underestimated westerly wind changes. *Nat. Commun.*, **7**, 10409, https://doi.org/10.1038/ncomms10409.

——, M. H. England, W. Cai, A. Sullivan, and P. J. Durack, 2018: Impacts of broad-scale surface freshening of the Southern Ocean in a coupled climate model. *J. Climate*, **31**, 2613–2632, https://doi.org/10.1175/JCLI-D-17-0092.1.

Purkey, S. G., and G. C. Johnson, 2010: Warming of global abyssal and deep Southern Ocean waters between the 1990s and 2000s: Contributions to global heat and sea level rise budgets. *J. Climate*, **23**, 6336–6351, https://doi.org/10.1175/2010JCLI3682.1.

Rhein, M., and Coauthors, 2013: Observations: Ocean. *Climate Change 2013: The Physical Science Basis*, T. F. Stocker et al., Eds., Cambridge University Press, 255–316.

Roemmich, D., and J. Gilson, 2009: The 2004–2008 mean and annual cycle of temperature, salinity, and steric height in the global ocean from the Argo program. *Prog. Oceanogr.*, **82**, 81–100, https://doi.org/10.1016/j.pocean.2009.03.004.

——, J. Church, J. Gilson, D. Monselesan, P. Sutton, and S. Wijffels, 2015: Unabated planetary warming and its ocean structure since 2006. *Nat. Climate Change*, **5**, 240–245, https://doi.org/10.1038/nclimate2513.

Russell, J. L., K. W. Dixon, A. Gnanadesikan, R. J. Stouffer, and J. R. Toggweiler, 2006: The Southern Hemisphere westerlies in a warming world: Propping open the door to the deep ocean. *J. Climate*, **19**, 6382–6390, https://doi.org/10.1175/JCLI3984.1.

Rye, C. D., J. Marshall, M. Kelley, G. Russell, L. S. Nazarenko, Y. Kostov, G. A. Schmidt, and J. Hansen, 2020: Antarctic glacial melt as a driver of recent Southern Ocean climate trends. *Geophys. Res. Lett.*, **47**, e2019GL086892, https://doi.org/10.1029/2019GL086892.

Sen Gupta, A., A. Santoso, A. S. Taschetto, C. C. Ummenhofer, J. Trevena, and M. H. England, 2009: Projected changes to the Southern Hemisphere ocean and sea ice in the IPCC AR4 climate models. *J. Climate*, **22**, 3047–3078, https://doi.org/10.1175/2008JCLI2827.1.

Seviour, W. J. M., A. Gnanadesikan, and D. W. Waugh, 2016: The transient response of the Southern Ocean to stratospheric ozone depletion. *J. Climate*, **29**, 7383–7396, https://doi.org/10.1175/JCLI-D-16-0198.1.

Shi, J.-R., S.-P. Xie, and L. D. Talley, 2018: Evolving relative importance of the Southern Ocean and North Atlantic in anthropogenic ocean heat uptake. *J. Climate*, **31**, 7459–7479, https://doi.org/10.1175/JCLI-D-18-0170.1.

Spence, P., J. C. Fyfe, A. Montenegro, and A. J. Weaver, 2010: Southern Ocean response to strengthening winds in an eddy-permitting global climate model. *J. Climate*, **23**, 5332–5343, https://doi.org/10.1175/2010JCLI3098.1.

Stössel, A., D. Notz, F. A. Haumann, H. Haak, J. Jungclaus, and U. Mikolajewicz, 2015: Controlling high-latitude Southern Ocean convection in climate models. *Ocean Modell.*, **86**, 58–75, https://doi.org/10.1016/j.ocemod.2014.11.008.

Swart, N. C., and J. C. Fyfe, 2012: Observed and simulated changes in the Southern Hemisphere surface westerly wind-stress. *Geophys. Res. Lett.*, **39**, L16711, https://doi.org/10.1029/2012GL052810.

——, and ——, 2013: The influence of recent Antarctic ice sheet retreat on simulated sea ice area trends. *Geophys. Res. Lett.*, **40**, 4328–4332, https://doi.org/10.1002/grl.50820.

——, ——, N. Gillett, and G. J. Marshall, 2015: Comparing trends in the southern annular mode and surface westerly jet. *J. Climate*, **28**, 8840–8859, https://doi.org/10.1175/JCLI-D-15-0334.1.

——, S. T. Gille, J. C. Fyfe, and N. P. Gillett, 2018: Recent Southern Ocean warming and freshening driven by greenhouse gas emissions and ozone depletion. *Nat. Geosci.*, **11**, 836–841, https://doi.org/10.1038/s41561-018-0226-1.

Tatebe, H., and Coauthors, 2019: Description and basic evaluation of simulated mean state, internal variability, and climate sensitivity in MIROC6. *Geosci. Model Dev.*, **12**, 2727–2765, https://doi.org/10.5194/gmd-12-2727-2019.

Thompson, D. W. J., 2002: Interpretation of recent Southern Hemisphere climate change. *Science*, **296**, 895–899, https://doi.org/10.1126/science.1069270.

Waugh, D. W., F. Primeau, T. Devries, and M. Holzer, 2013: Recent changes in the ventilation of the southern oceans. *Science*, **339**, 568–570, https://doi.org/10.1126/science.1225411.

Yukimoto, S., and Coauthors, 2019: The Meteorological Research Institute Earth System Model version 2.0, MRI-ESM2.0: Description and basic evaluation of the physical component. *J. Meteor. Soc. Japan*, **97**, 931–965, https://doi.org/10.2151/jmsj.2019-051.

Zhang, L., T. L. Delworth, W. Cooke, and X. Yang, 2019: Natural variability of Southern Ocean convection as a driver of observed climate trends. *Nat. Climate Change*, **9**, 59–65, https://doi.org/10.1038/s41558-018-0350-3.

Zika, J. D., and Coauthors, 2013: Vertical eddy fluxes in the Southern Ocean. *J. Phys. Oceanogr.*, **43**, 941–955, https://doi.org/10.1175/JPO-D-12-0178.1.